

Article

Aminated Spherical SiO₂ Synthesized from Fly Ash and Its Application for Pb²⁺ and Cu²⁺ Sorption

Jiahui Chen ^{1,2}, Nengsheng Liu ^{3,*}, Yunzhu Wang ², Xiang Li ², Zheren Zhang ^{1,2}, Le Liu ³, Zhaoyang Dou ¹ and Sufang He ^{1,2,*}

¹ Faculty of Materials Science and Engineering, Kunming University of Science and Technology, Kunming 650093, China

² Research Center for Analysis and Measurement, Kunming University of Science and Technology, Kunming 650093, China

³ Faculty of Metallurgical and Energy Engineering, Kunming University of Science and Technology, Kunming 650093, China

* Correspondence: liunengsheng@kust.edu.cn (N.L.); sufanghe@kust.edu.cn (S.H.)

Abstract: Fly ash was utilized as raw material for the preparation of spherical SiO₂ (SS), which was subsequently ammonified using APTES (H₂NCH₂CH₂CH₂Si(OC₂H₅)₃) to obtain aminated spherical SiO₂ (SSN). The physicochemical properties of SS and SSN were systematically characterized. Notably, SS exhibited a remarkable specific surface area and pore volume, enabling it to accommodate abundant nitrogen-containing groups. These functional groups served as crucial active sorption sites, significantly enhancing the sorption capacity of SiO₂ for Pb²⁺ and Cu²⁺ ions. Thus, the removal efficiency was above 99.9% when using dosages of 4 and 6 g/L SSN in solutions containing 200 mg/L of Pb²⁺ and Cu²⁺, respectively. Additionally, SSN showed a higher theoretical maximum sorption capacity for Pb²⁺ and Cu²⁺ ions, as determined by the Langmuir isotherm model, with values of 185.2 mg/g and 86.2 mg/g, respectively. These results surpass those reported in previous studies on adsorbents derived from fly ash. The chemical reactions that occurred between the aqueous cations and nitrogen-containing groups were identified as the pivotal factors governing the sorption of Pb²⁺ and Cu²⁺. This study presents a practical approach to fly ash utilization, along with the effective removal of Pb²⁺ and Cu²⁺ from water.

Keywords: fly ash; spherical silica; sorption; heavy metal treatment



Citation: Chen, J.; Liu, N.; Wang, Y.; Li, X.; Zhang, Z.; Liu, L.; Dou, Z.; He, S.. Aminated Spherical SiO₂ Synthesized from Fly Ash and Its Application for Pb²⁺ and Cu²⁺ Sorption. *Water* **2024**, *16*, 1149. <https://doi.org/10.3390/w16081149>

Academic Editor: José Alberto Herrera-Melián

Received: 14 March 2024

Revised: 14 April 2024

Accepted: 15 April 2024

Published: 18 April 2024



Copyright: © 2024 by the authors. Licensee MDPI, Basel, Switzerland. This article is an open access article distributed under the terms and conditions of the Creative Commons Attribution (CC BY) license (<https://creativecommons.org/licenses/by/4.0/>).

1. Introduction

Heavy metal ions, particularly Pb²⁺ and Cu²⁺, are significant water contaminants due to their widespread distribution, non-biodegradability, and toxicity, which can result in varying degrees of harm to human health. [1]. Various strategies have been developed for the removal of these toxic metal ions from water, including chemical precipitation, ion exchange, membrane filtration coagulation/flocculation, electrochemical treatment, and sorption [2]. The sorption method has gained increasing attention due to its straightforward operation and exceptional removal efficacy [3]. However, the exorbitant cost of conventional adsorbents poses a significant challenge that must be addressed [4,5]. Therefore, the investigation of low-cost adsorbents synthesized from industrial waste has garnered significant interest [6–8].

Fly ash (FA), a prominent industrial solid waste generated in metallurgy, thermal power, the chemical industry, and other sectors, not only occupies significant space in the natural environment, but also poses severe respiratory health risks due to its propensity for dusting. Therefore, finding a rational solution for the disposal of this industrial solid waste is an urgent issue that demands attention [9,10]. One approach to address the disposal of FA is to enhance its added value through scientific research for its application elsewhere [11]. A proven method for the treatment of fly ash involves utilizing it as

an economically viable raw material for synthesizing silicon-based materials due to its abundant Si component. Among silicon-based materials, spherical SiO_2 exhibits promising characteristics as a porous material, due to its exceptional structural stability and high specific surface area, which signifies its immense potential in pollutant sorption [12–14]. However, despite possessing a competent pore structure, pure SiO_2 consistently exhibits inadequate sorption capacity for heavy metal ions [15]. McManamon et al. [16] synthetized spherical SiO_2 with a considerably high specific surface area ($871 \text{ m}^2/\text{g}$). However, the sorption capacity of Pb^{2+} was limited to only 18 mg/g . This poor sorption ability is attributed to the insufficient presence of surface active complexation sites, resulting in predominantly electrostatic or hydrogen bond interactions for bonding most heavy metal species [6]. Therefore, it is imperative to employ an effective modification method for enhancing the sorption capacity of SiO_2 . Based on previous studies, the amino (-NH₂) group has demonstrated a significant complexation ability towards heavy metal species, such as Pb^{2+} , Cu^{2+} , HCrO_4^- , and $\text{Cr}_2\text{O}_7^{2-}$ [17–19]. Meanwhile, a previous study has demonstrated the viability of ammoniation modification for SiO_2 , indicating its effectiveness [12]. Hence, in this work, we propose a novel approach wherein fly ash is utilized as a silicon source and the extraction of silicon is achieved through high-temperature activation with Na_2CO_3 , followed by acid leaching and alkaline leaching. Subsequently, P123 is employed as a template agent for the synthesis of spherical SiO_2 . And then, the SiO_2 surface is modified using 3-aminopropyl-tri-ethoxy-silane (APTES) to introduce nitrogen-containing groups. Furthermore, the physicochemical properties, and the Pb^{2+} and Cu^{2+} sorption ability of spherical SiO_2 , and the ammoniation of SiO_2 , are analyzed.

The present study employs the one-step reflux condensation method to modify industrial waste-derived SiO_2 in order to obtain aminated SiO_2 , which exhibits high efficiency in adsorbing Pb^{2+} and Cu^{2+} ions from aqueous solutions.

2. Experiments

2.1. Materials

Fly ash (FA) was collected from the thermal power plants operated by Inner Mongolia Datang International Togtoh Power Generation, Co., Ltd. (Hohhot, China).

The chemicals, namely sodium carbonate (Na_2CO_3), sodium hydroxide (NaOH), nitric acid (HNO_3), and hydrochloric acid (HCl), were procured from China National Medicines Co., Ltd., Shanghai, China. The 3-aminopropyl-tri-ethoxy-silane (APTES, Mw = 221.37) was obtained from Shanghai Macklin Biochemical Co., Ltd., Shanghai, China. Copper sulphate (CuSO_4) and lead nitrate ($\text{Pb}(\text{NO}_3)_2$) were purchased from Tianjin Fengchuan Chemical Reagent Technology Co., Ltd., Tianjin, China. All the chemical reagents used in this study were of analytical reagent grade and required no further purification.

2.2. Preparation of the Samples

Fly ash (FA) weighing 100 g was mixed with 100 g of Na_2CO_3 powder and, subsequently, subjected to calcination in a muffle furnace at a heating rate of $25 \text{ }^\circ\text{C}/\text{min}$, reaching a peak temperature of $900 \text{ }^\circ\text{C}$, and held for a duration of 2 h. The resulting product was designated as FAC.

Then, 100 g FAC was soaked in 1000 mL of 50% HNO_3 for 12 h, and the filtering residue (named SP) was collected and utilized as a silicon precursor after vacuum filtration.

The SP (10 g) was mixed with 100 mL of NaOH solution (15% mass fraction), followed by heating in an oil bath at $100 \text{ }^\circ\text{C}$ for 1 h. Subsequently, the mixture was separated using high-speed centrifugation and the resulting supernatant was collected. Then, the supernatant (7.4 g) was mixed with deionized water (22 g) and added, dropwise, to a solution composed of P123 (polyethylene oxide–polypropylene oxide–polyethylene oxide, 2 g) and 2 mol/L HCl (60 g). The resulting mixture was then transferred to a high-pressure autoclave and heated at $100 \text{ }^\circ\text{C}$ for 24 h. After natural cooling, the product was washed, filtered, dried, and ground. The obtained SiO_2 material was designated as SS. The aminated silica material was synthesized as follows: a mixture of 0.5 g of SS, 50 mL of absolute

alcohol, and 1.25 mL of APTES ($\text{H}_2\text{NCH}_2\text{CH}_2\text{CH}_2\text{Si}(\text{OC}_2\text{H}_5)_3$) was subjected to ultrasonic oscillation for 50 min. Subsequently, the mixture was stirred and refluxed at 50 °C for 6 h. Afterwards, the suspension underwent five washes with absolute alcohol, followed by centrifugation in order to achieve separation. The resulting powder was collected and designated as SSN.

2.3. Characterization

The raw material components (FA) were analyzed using X-ray fluorescence (XRF-1800, Shimadzu, Kyoto, Japan), with an instrument working voltage of 40 kV and a working current of 95 mA, at a flow rate of 8 mL min^{-1} . The X-ray diffraction (XRD) patterns were measured using an X-ray diffractometer (BRUKER D8, Bruker, Madison, WI, USA), with Cu K α radiation ($\lambda = 1.5406 \text{ \AA}$), operating at 40 kV and 30 mA. The scanning speed was 8 °/min, and the scanning range was 0°–80°. The acceleration voltage of the scanning electron microscopy (SEM, Nova NanoSEM 450, FEI, Hillsboro, OR, USA) was 50 V–30 kV and the magnification was 20–1000 k. An automatic adsorption instrument (ASAP-2460, Micromeritics, Norcross, GA, USA) was used to determine the N_2 adsorption–desorption isotherms. The specific surface area was calculated using the Barrett–Emmett–Teller (BET) method, and the pore volume and pore size distribution were calculated using the Barrett–Joyner–Halenda (BJH) method. Fourier transform infrared (FT-IR) spectroscopy was conducted via an infrared absorption spectrometer (Nicolet 560 IR, Thermo Nicolet, Waltham, MA, USA). The scanning range of the spectrum was 4000–400 cm^{-1} . The elemental composition of the fresh and used adsorbents was analyzed using X-ray photoelectron spectroscopy (XPS, ESCALAB250Xi, Thermo Scientific, Waltham, MA, USA). Thermogravimetric analysis was performed under a nitrogen atmosphere with Setaram equipment (TGA-DTA, STA449F3 Jupiter, Netzsch, Bavaria, Germany); the samples were heated from 40 to 810 °C at 10 °C/min and the sample mass introduced was 25 mg. The concentrations of various elements in the solutions were analyzed by an inductively coupled plasma spectrometer (ICP-OES, Prodigy, Teledyne Leeman Labs, Hudson, NH, USA).

The point of zero charge (pHpzc) of SS and SSN was determined through the modified pH drift method. According to which 0.05 g of SS (or SSN) was put into a beaker and mixed with 50 mL of different NaNO_3 solutions, of which the concentration was 0.01 mol/L, and the initial pH was adjusted at 1, 2, 3, 4, and 5, respectively. The mixtures were stirred at room temperature for 24 h. The pH_{pzc} accords to the pH value, where the curve crosses the line of $\text{pH}_{\text{initial}} = \text{pH}_{\text{final}}$.

2.4. Sorption Experiments

The Pb^{2+} and Cu^{2+} solutions with different concentrations were prepared by dissolving agent $\text{Pb}(\text{NO}_3)_2$ and $\text{CuSO}_4 \cdot 5\text{H}_2\text{O}$ in deionized water, in which the pH value was adjusted by 0.1 mol/L NaOH and 0.1 mol/L H_2SO_4 (or HNO_3).

The sorption experiments were conducted on sample SS and SSN. Briefly, 50 mL of Pb^{2+} and Cu^{2+} solution (200 mg/L) were mixed with 0.05 g of the adsorbent and put into conical flasks and stirred with a magnetic stirrer at room temperature for 4 h.

To investigate the effect of the contact time, sorbent dosage, initial pH, and solution concentration on the sorption behavior, further sorption experiments were carried out on SSN as a representative. The experimental conditions were as following: sorbent amount of 0.025, 0.05, 0.10, 0.20, and 0.40; initial pH of 1, 2, 3, 4, and 5; contact time of 5, 10, 30, 60, 90, 120, and 240 min; Pb^{2+} (or Cu^{2+}) concentration of 20, 50, 80, 120, 150, 180, and 200 mg/g, respectively.

All of the sorption experiments were conducted in triplicate, and the average values were reported. The corresponding error bars for the values were determined.

The suspensions were separated by centrifugation, and then filtered after the sorption experiments. The concentrations of Pb^{2+} or Cu^{2+} in the solutions before and after sorption

were determined by ICP-OES. The Pb^{2+} or Cu^{2+} sorption ability was evaluated using the following Equations (1) and (2):

$$q = \frac{(c_0 - c_t) \times v}{m} \quad (1)$$

$$\eta = \frac{c_0 - c_t}{c_0} \times 100\% \quad (2)$$

where q (mg/g) means the sorption capacity, v (L) means the solution volume, m (g) means the mass of the adsorbent, η (%) means the pollutant removal efficiency, C_0 (mg/L) means the initial concentration of the pollutant (Pb^{2+} or Cu^{2+}), C_t (mg/L) means the concentration at the time t (min).

The sorption kinetic models were plotted according to pseudo-first-order model and pseudo-second-order model [20]. And the isotherm parameters were plotted according to the Langmuir and Freundlich models [21,22]. The details are provided by the following Equations (3)–(6):

$$\text{Pseudo-first-order model (PF)} : \ln(q_e - q_t) = \ln q_e - k_1 \times t \quad (3)$$

$$\text{Pseudo-second-order model (PS)} : \frac{t}{q_t} = \frac{1}{k_2 \times q_e^2} + \frac{t}{q_e} \quad (4)$$

where t (min) means the sorption time, Q_e (mg/g) and q_t (mg/g) mean the equilibrium sorption capacity and the sorption capacity at the sorption time, k_1 and k_2 (min^{-1}) are constant coefficients of the pseudo-first-order and the pseudo-second-order kinetic equation. With t utilized as the horizontal coordinate and $\ln(q_e - q_t)$ (or t/q_t) used as the vertical coordinate, the linear fits are plotted to the resulting data, in which the corresponding kinetic parameters are analyzed as follows:

$$\text{Langmuir isotherm} : \frac{c_e}{q_e} = \frac{1}{q_m \times k_l} + \frac{c_e}{q_m} \quad (5)$$

$$\text{Freundlich isotherm} : \log q_e = \log k_f + \frac{1}{n} \log c_e \quad (6)$$

where q_e (mg/g) is the equilibrium sorption capacity and c_e (mg/L) is the equilibrium concentration after the sorption process, q_m (mg/g) is the maximum sorption capacity, k_l and k_f are the Langmuir constant and Freundlich constant, respectively, and $1/n$ is the intensity of the sorption.

3. Results and Discussion

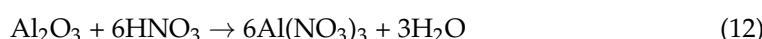
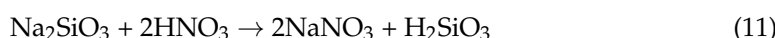
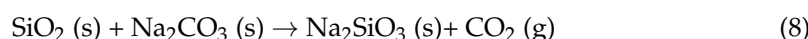
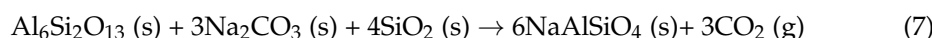
3.1. Physicochemical Properties

The chemical composition of FA and SP were determined by X-ray fluorescence (XRF), and the results are displayed in Table 1; FA mainly consists of Si and Al components, with SiO_2 and Al_2O_3 content of 37.40% and 46.22%, respectively. Comparatively, the content of Al_2O_3 and other metallic oxides in SP were significantly decreased, of which the content of Al_2O_3 was reduced to 4.46%, and the contents of Fe_2O_3 and CaO were reduced to below 1%. Meanwhile, the content of SiO_2 steeply increased to 79.65%. These findings indicate that most of the impurities in FA were effectively removed through Na_2CO_3 mixed high-temperature activation combined with HNO_3 leaching, making SP a promising silicon precursor.

Table 1. Average chemical composition of original fly ash (FA) and silicon precursor (SP).

Sample	Component (%)				
	SiO_2	Al_2O_3	Fe_2O_3	CaO	TiO_2
FA	37.40	46.22	3.05	5.17	3.51
SP	79.65	4.46	0.12	0.43	2.27

To further elucidate the evolving trends in the phase composition during the preparation process, X-ray diffraction analysis was conducted on samples FA, FAC, SP, SS, and SSN. The corresponding results are presented in Figure 1. The presence of a significant amount of mullite ($\text{Al}_6\text{Si}_2\text{O}_{13}$), along with Al_2O_3 and SiO_2 , was observed in FA (Figure 1a). FAC, on the other hand, consisted of NaAlSiO_4 , Na_2SiO_3 , and Al_2O_3 (Figure 1b). The observed changes can be attributed to the successful transformation of $\text{Al}_6\text{Si}_2\text{O}_{13}$ into Al_2O_3 and NaAlSiO_4 , as well as the conversion of SiO_2 into Na_2SiO_3 during the high-temperature activation process, with a mixture of Na_2CO_3 (the related reaction equations are described in Equations (7)–(9)) [23]. In the SP pattern, shown in Figure 1c, a prominent broad peak around 25° was observed, which can be attributed to the presence of amorphous SiO_2 . Additionally, minor interfering peaks were exclusively detected, as shown in Figure 1c, indicating the existence of residual metallic oxides and inorganic salts. The results indicated that the removal of metallic oxide and inorganic salt from FAC, as well as the sufficient transformation of Si species into SiO_2 , were achieved through a series of processes including HNO_3 leaching, filtering, and drying (the related reaction equations are described in Equations (7)–(13)) [24]. Additionally, following P123 treatment, the phase curve exhibited enhanced smoothness and the interfering peaks in regard to SS were eliminated (as shown in Figure 1c), indicating further purification of the SiO_2 component. Moreover, SSN (in Figure 1c) exhibited similar phases to SS, with slight shifting and widening observed in the characteristic peak of SiO_2 , which could be attributed to NH_2 group grafting [9]. Meanwhile, based on the small angle XRD pattern of SS (in Figure 1d), a prominent characteristic peak near 1° was observed, indicating the presence of an ordered mesoporous structure. However, following ammoniation modification, this peak exhibited a noticeable reduction in intensity and shifted towards larger angles. This phenomenon may be attributed to the obstruction of the pore structure caused by residual APTES macromolecules.



The SEM images of SS and SSN are exhibited in Figure 2. According to the SEM images in Figure 2a,b, SS exhibited the successful synthesis of a spherical structure with a uniform particle size, utilizing P123 as the template agent. In contrast, the ammoniation modification of SSN maintained its spherical structure, but resulted in a larger and more uneven particle size, along with an increased agglomeration tendency (in Figure 2c,d).

To further investigate the effectiveness of ammoniation modification and explore the physicochemical properties of SS and SSN, comprehensive analysis, including FTIR, XPS, and TGA, was conducted on these samples. The corresponding results are presented in Figure 3.

Figure 3a displays the FTIR spectra of SS and SSN, wherein the wide and intense bands around 3450 cm^{-1} can be attributed to the stretching vibrations of the -OH bonds [25], the peaks observed at 1640 cm^{-1} can be attributed to the absorption of free water molecules [26], the characteristic peaks at 1098 and 800 cm^{-1} are indicative of the Si–O–Si bonds, while the bond stretching vibration of Si–OH is attributed to the peak observed at 963 cm^{-1} [27]. The characteristic peak in the SSN spectra near 2950 cm^{-1} implied the existence of -CH₂- groups apart from the residual APTES macromolecules [28,29]. In addition, the sorption peak near 1539 cm^{-1} and 1350 cm^{-1} belonged to the -NH₂ and -CH groups on the surface, as well as the peak near 694 cm^{-1} , which was attributed to the -NH- group that had sub-

stituted the oxygen atom in the skeleton of SSN [30]. The presence of nitrogen-containing functional groups on SS was confirmed through the successful grafting after the APTES treatment. Additionally, the ammoniation modification resulted in a significant decrease in the adsorption peak of Si–OH, indicating the effective coverage of the SiO_2 surface by the nitrogen-containing groups.

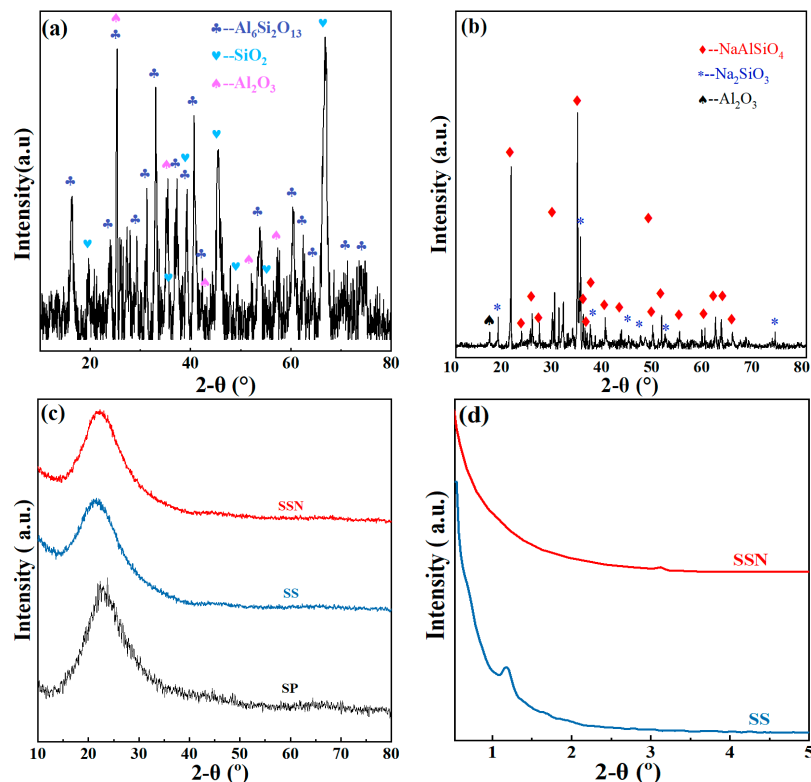


Figure 1. XRD pattern of: (a) FA (large angle), (b) FAC (large angle), (c) SP, SS, and SSN (large angle), (d) SS and SSN (small angle).

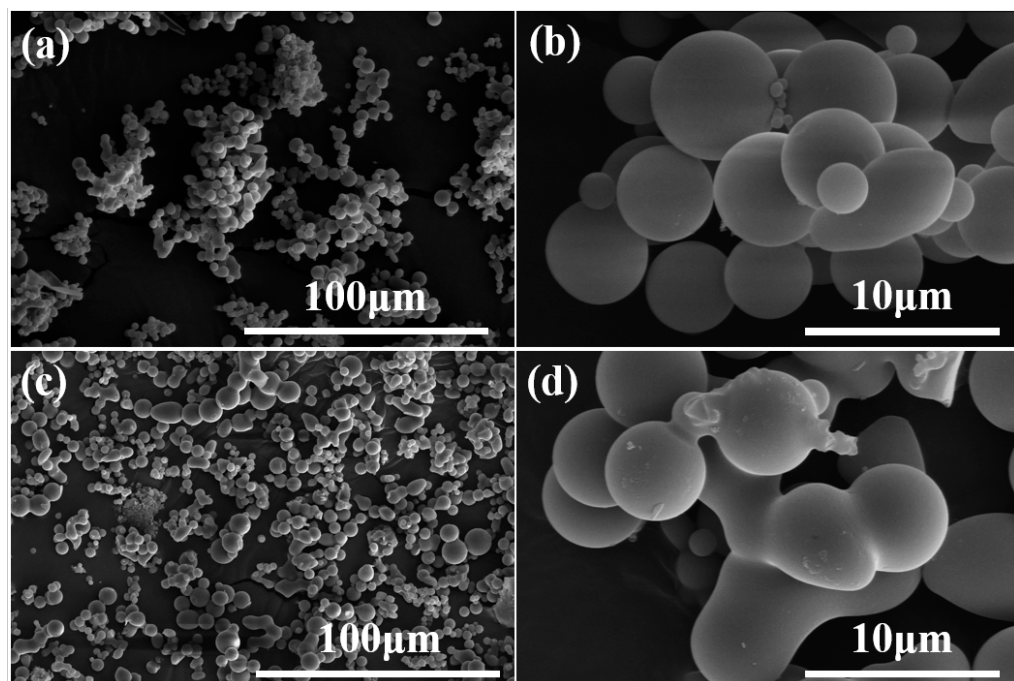


Figure 2. SEM images of: (a,b) SS, (c,d) SSN.

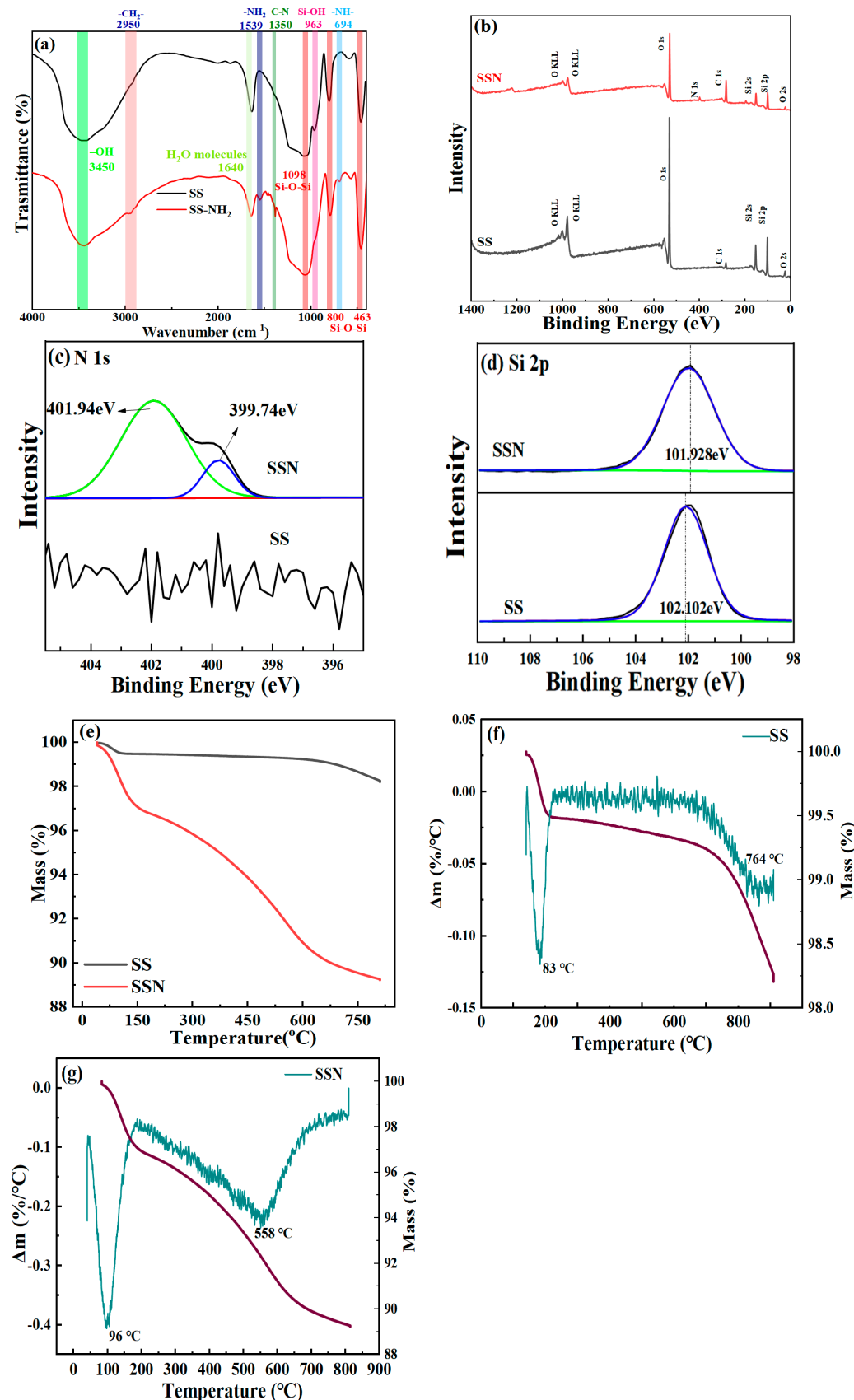


Figure 3. FTIR, XPS, TGA, and DTG spectra: (a) FTIR spectra of SS and SSN, (b–d) XPS spectra of SS and SSN, (e) TGA spectra of SS and SSN, (f) TGA and DTG spectra of SS, (g) TGA and DTG spectra of SSN.

XPS analysis was utilized to determine the chemical environment of the elemental composition of Si and N on SS and SSN, and the spectra are exhibited in Figure 3b–d. The survey spectra presented in Figure 3b reveals the presence of a subtle N 1s characteristic peak within the SSN. In Figure 3c, the characteristic peaks of 401.94 eV and 399.74 eV represent the -NH_3^+ and -NH_2 groups on the surface of the SSN [31]. In comparison, no apparent characteristic peak of the N element could be observed in SS, which further indicated that the nitrogen-containing functional groups found in the spectra of SSN were introduced by the APTES modification. The Si 2p spectra are shown in Figure 3d, in which the characteristic peak of SiO_2 (101.93 eV) has been reduced and has shifted slightly to lower the energy level after the ammoniation modification process, which could be attributed to the cover of the -NH_3^+ and -NH_2 groups [6].

The curves of the TG and DTG analysis are shown in Figure 3, which provide information on the composition and thermal stability. Evidently, SS exhibited three stages of weightlessness (Figure 3e). In the first stage, desorption of the absorbed water molecules and surface hydroxyl radicals occurred within the temperature range of 40 to 120 °C, resulting in a weight loss of 0.504%. This weight loss corresponded to the peak observed around 83 °C on the derivative thermogravimetric (DTG) curves. And then, in the second stage (120 to 594 °C), a weight loss of 0.241% was ascribed to the polycondensation of amorphous SiO_2 . In the last stage (594 to 810 °C), a weight loss of 1.048% was observed. Meanwhile, the weight loss trend of SSN was divided into three stages (Figure 3f). The first stage, in the range of 40 to 130 °C, which corresponded to the temperature on the DTG curves of 96 °C, was ascribed to the desorption of the absorbed water molecules and surface hydroxyl radicals. This stage caused a weight loss of 2.961%. The second stage, created by the decomposition of NH_2 groups and the polycondensation of amorphous SiO_2 at 558 °C (in the range of 130 to 600 °C), caused 6.872% of weight loss, which further provided NH_2 groups on the surface of SSN. In the third stage (600 to 810 °C), the NH_2 groups have been decomposed completely, but the polycondensation of amorphous SiO_2 was still in progress and caused a weight loss of 0.939%. In summary, sample SS and SSN exhibited a huge difference in regard to their thermal stability, of which there was a weight loss of 1.793% and 10.772% in the range of 40 to 810 °C, respectively. The wide variations in weight loss may be attributed to the decomposition of nitrogen-containing groups during the heating process.

To evaluate the effect of the APTES treatment, the grafting percentage and the conversion ratio of the monomer to polymer were determined through Equations (14) and (15), which is relevant to the results from the curves in the TGA analysis [28].

$$G = \frac{m_s - m_N}{m_N} \times 100\% \quad (14)$$

$$\text{Conversion} = \frac{G \times W_M}{W_s} \times 100\% \quad (15)$$

where G (%) is the grafting percentage, m_s (%) and m_N (%) are the ash content of SS and SSN after the TGA analysis, Conversion (%) means the conversion ratio of the monomer to polymer, W_M (g) and W_s (g) are the mass of the APTES and SS used in the synthesis process.

By doing the calculations, the grafting percentage is 10.04% and the conversion ratio of the monomer to polymer is 23.80%, indicating that the nitrogen-containing functional groups have been successfully grafted onto the SSN.

The specific surface area and pore structure parameters of SS and SSN were determined, and the results are given in Table 2. SS shows a high specific surface area ($677.5 \text{ m}^2/\text{g}$) and pore volume ($0.023 \text{ cm}^3/\text{g}$). The competent pore structure parameter of SS might be due to its spherical structure, which indicates its efficiency in carrying nitrogen-containing groups [16]. In addition, the specific surface area was observed to decrease to $351.2 \text{ m}^2/\text{g}$, accompanied by a reduction in the total pore volume to $0.012 \text{ m}^2/\text{g}$ and a decrease in the average pore diameter to 3.07 nm , following the ammoniation modification. The observed decrease can be attributed to the pore blockage caused by residual APTES

macromolecules. The N_2 adsorption–desorption isotherms of SS and SSN are displayed in Figure 4a,b, in which both of these corresponded to type IV isotherms, indicating the mesoporous structure of SS and SSN [9]. In addition, according to the pore size distribution curves (in Figure 4a,b), sample SS and SSN showed a uniform pore distribution, which primarily ranged within approximately 3 nm. The point of zero charge (pHpzc) of SS and SSN were determined and are exhibited in Table 2. SS showed a low pH_{pzc} (2.62), and the reported similarity of this value to that of other pure SiO_2 in previous studies can be attributed to the presence of Si–OH groups, which readily undergo deprotonation for the capture of OH[−] ions (as in Equation (14)) [9]. In contrast, SSN shows a noticeably higher pH_{pzc}. The observed increase can be attributed to the introduction of -NH₂ groups, which exhibit a greater propensity for protonation in solution (as in Equation (15)) [32]. In brief, SS and SSN had a relatively low pH_{pzc} value and, thus, could be negatively charged in water, and could easily attract heavy metal cations, in theory [32].



Table 2. The specific surface area (SSA), total pore volume (PV), average pore diameter (PD), and zero-point potential (pH_z) of SS and SSN.

Sample	SSA (m^2/g)	PV (cm^3/g)	PD (nm)	pH _{pzc}
SS	677.5	0.023	3.42	2.62
SSN	351.4	0.012	3.07	3.64

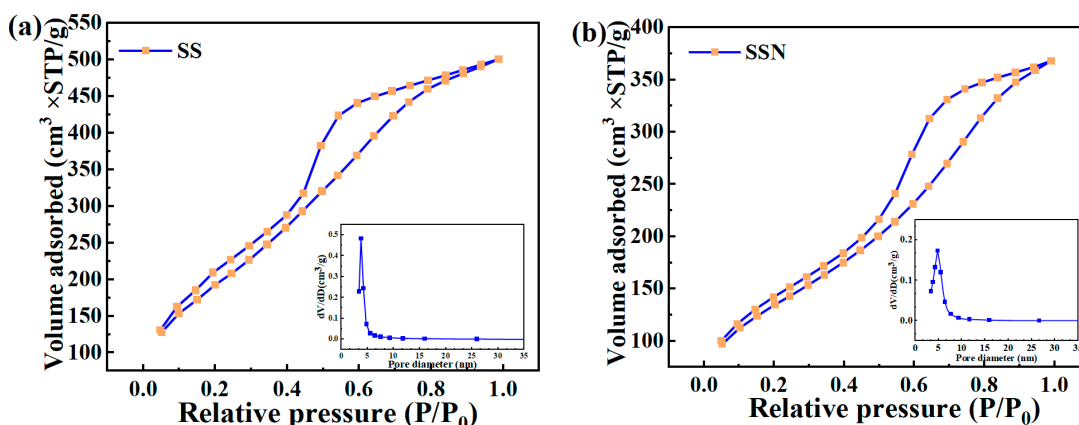


Figure 4. N_2 adsorption–desorption isotherms and pore size distribution curves of: (a) SS, (b) SSN.

3.2. Sorption Ability and Behavior

3.2.1. Batch Sorption Experiment

In order to investigate the Pb²⁺ and Cu²⁺ removal efficiency by SS and SSN, batch sorption experiments were conducted. The results showed that the sorption capacity of SS for Pb²⁺ was 2.4 mg/g, while that of SSN was significantly higher at 106.0 mg/g (Figure 4). Similarly, the sorption capacity of SS for Cu²⁺ was found to be 2.0 mg/g, whereas SSN exhibited a higher sorption capacity of 62.2 mg/g. Obviously, the ammoniation modification had significantly improved the Pb²⁺ and Cu²⁺ sorption ability of SiO_2 (SS), of which the Pb²⁺ and Cu²⁺ sorption capacity had increased 44.2 times and 31.1 times, respectively. After conducting the aforementioned analysis, SS had a low pH_{pzc} and tended to undergo deprotonation for attracting cations. However, it lacked active sites for fixing Pb²⁺ and Cu²⁺, thereby resulting in its limited sorption capacity [16]. Although the specific surface area and pore volume of SSN had drastically decreased compared to SS, the ammoniation modification had added the -NH₂ groups to the surface and provided many of the active sorption sites for fixing Pb²⁺ and Cu²⁺ [7]. Meanwhile, it can be inferred

that the Si-OH and -Si- groups exhibit limited sorption ability towards Pb^{2+} and Cu^{2+} , while the nitrogen-containing groups account for the remarkable sorption capacity of SSN towards Pb^{2+} and Cu^{2+} . By doing the calculations, the Pb^{2+} and Cu^{2+} sorption capacity of SSN (106.0 mg/g and 62.2 mg/g) could be converted into 0.51 mmol/g and 0.97 mmol/g, respectively. Obviously, more Cu^{2+} cations were captured than Pb^{2+} cations. This may be owing to the ionic radius of Cu^{2+} (0.73 Å), which is that much smaller than the value of Pb^{2+} (1.19 Å), for which the Cu^{2+} cations could be transferred and diffused in the pore structure of the adsorbent more easily.

3.2.2. Further Sorption Experiments

Effect of Different Factors

In order to investigate the effect of the sorbent dosage on the Pb^{2+} and Cu^{2+} removal efficiency, the dosage of SSN of 0.05, 0.1, 0.2, 0.3, and 0.4 g was adopted to carry out the sorption experiments, with 50 mL of Pb^{2+} and Cu^{2+} solution (200 mg/L), for 240 min. And as shown in Figure 5 the removal efficiency increased gradually due to the increase in the sorbent dosage, and the value of Pb^{2+} and Cu^{2+} went from 57.03% and 22.53% to above 99.9% when the sorbent dosage at 0.05 g rose to 0.2 g and 0.3 g, respectively (in Figure 6b), which might be due to the possibility that the increase in the sorbent dosage would provide more active sites [33]. The results indicated that the aminated SiO_2 synthesized from FA exhibited a remarkable ability to effectively remove Pb^{2+} and Cu^{2+} in high concentration solutions.

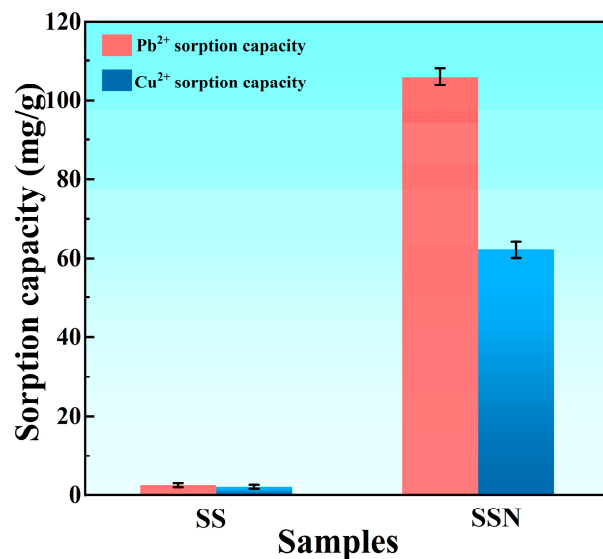


Figure 5. Pb^{2+} and Cu^{2+} removal ability of SS and SSN. Conditions: sorbent = 0.05 g, initial Pb^{2+} (or Cu^{2+}) concentration = 200 mg/L, sorption temperature = 25 °C, contact time = 4 h, and solution volume = 50 mL.

To investigate the impact of the contact time, sorbent dosage, solution pH, and initial concentration on the sorption behavior, a series of relevant sorption experiments were conducted using SSN. The mathematical relationship between the contact time and the Pb^{2+} and Cu^{2+} sorption ability of SSN is presented in Figure 6a. The relevant experimental conditions were as following: 0.05 g of SSN was put into 50 mL of Pb^{2+} and Cu^{2+} solutions in 200 mg/L, and the value of the sorption capacity for different contact times (for 1 to 240 min) was detected. Accordingly, the sorption capacity of Pb^{2+} exhibited rapid growth within the first 80 min, followed by a slower growth trend between 80 and 180 min. Finally, at 210 min, the maximum Pb^{2+} sorption capacity (106.0 mg/g) was achieved. Meanwhile, the Cu^{2+} sorption capacity showed a high increasing trend in the first 30 min, and then it became gentle until it reached the maximum (55.6 mg/g) at 210 min. The significant initial increase in the Pb^{2+} and Cu^{2+} sorption capacity can be attributed to the abundance of

active sites and heavy metal cations present in the solution. And, subsequently, the active sites and heavy metal cations in the solution reduced continuously due to the sorption process, which significantly decreased the opportunities for contact between the sorption sites and the adsorbate.

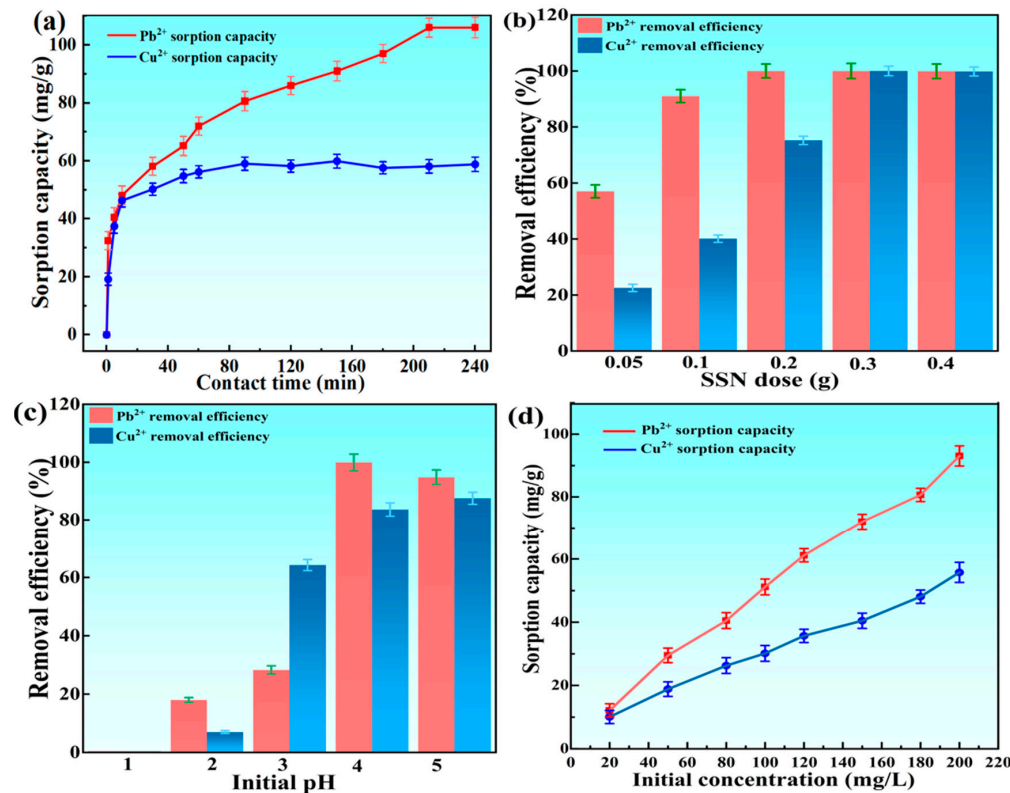


Figure 6. Effects of different factors on Pb^{2+} and Cu^{2+} sorption by SSN: (a) contact time, (b) sorbent dosage, (c) solution pH value, (d) adsorbate concentration.

The pH of the solution, which influences the surface charge of the sorbent and the speciation of heavy metals, plays a crucial role in the sorption process. [34]. To investigate this influence, sorption experiments were conducted using 50 mL of the Pb^{2+} and Cu^{2+} solutions, with an initial concentration of 200 mg/L, adjusted to a pH range of 1 to 5. A dosage of 0.2 g of SSN was employed for each experiment, with a duration of 240 min. The results of the experiments are displayed in Figure 6c; according to which SSN showed almost no sorption ability for Pb^{2+} and Cu^{2+} when the pH was 1. The subsequent increase in pH to 4 resulted in a sharp rise in the Pb^{2+} removal efficiency, exceeding 99.9%, which approached the equilibrium value for removal efficiency. Meanwhile, the Cu^{2+} removal efficiency exhibited a gradual increase to 5% within the pH range of 1 to 2. Subsequently, it experienced a sharp rise to 90.86 as the pH increased to 4 and, thereafter, demonstrated a smooth growth trend in regard to the removal efficiency with further increases in the pH. A higher pH value is beneficial for Pb^{2+} and Cu^{2+} sorption, as SSN exhibits a greater affinity for OH^- ions, facilitating deprotonation and cation attraction. [35].

Figure 6d illustrates the effect of the initial Pb^{2+} and Cu^{2+} concentrations on the sorption capacity, in which 0.05 g of SSN was used as an adsorbent to treat 50 mL of the Pb^{2+} and Cu^{2+} solution at pH 4 and 5, respectively, in different concentrations for 240 min. Clearly, the Pb^{2+} sorption capacity increase from 12.1 mg/g to 93.1 mg/g occurred due to the initial concentration increase from 20 mg/L to 200 mg/L; the Cu^{2+} sorption capacity increase from 10.6 mg/g to 55.8 mg/g occurred after the initial concentration increase from 20 mg/L to 200 mg/L. The sorption capacity significantly increased with the increase in the initial concentration, and no clear equilibrium value for the sorption capacity was observed

in the corresponding function. This suggests that an even higher sorption capacity could be achieved at higher concentrations of Pb^{2+} and Cu^{2+} cations.

Isotherm and Kinetics of Sorption

To further study the kinetic behavior and mechanisms in Pb^{2+} and Cu^{2+} sorption, the pseudo-first-order (PF-order) and pseudo-second-order (PS-order) models were used to fit the sorption experiments, and the results are exhibited in Figure 7a,b and Table 3. When the regression coefficient (R^2) of the formula PS-order is larger than this value for the PF-order, it is implied that the PS-order model fits to the sorption behavior better. The aforementioned examples demonstrate that the chemical reaction plays a pivotal role in constraining the rate of the steps involved in these sorption processes [36].

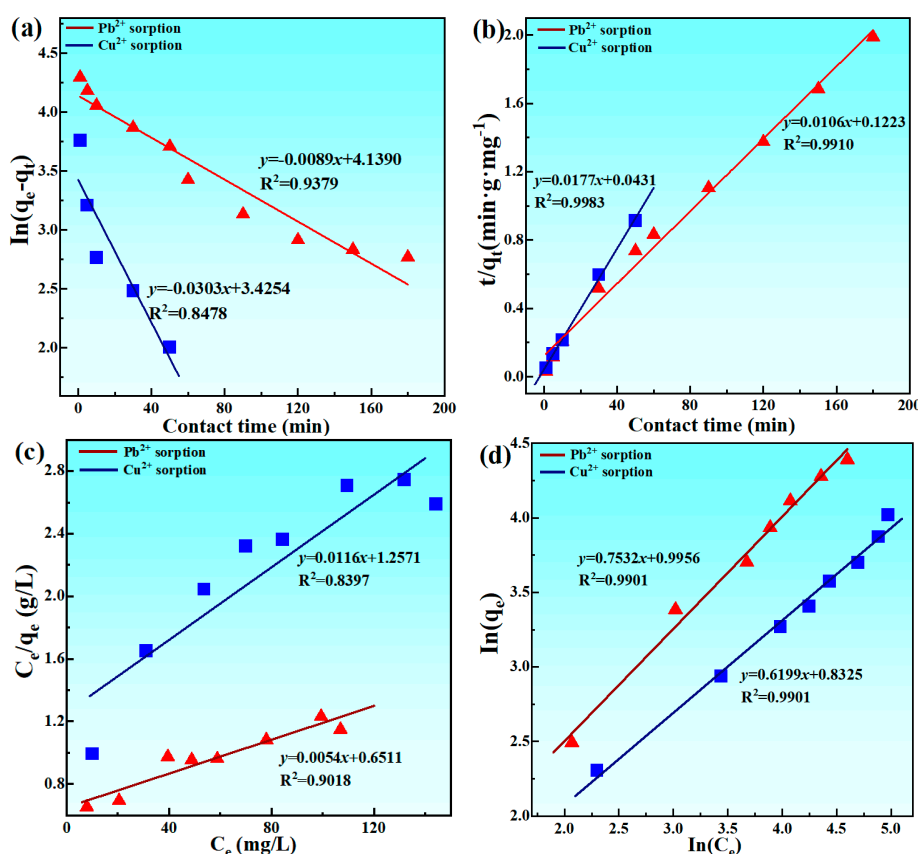


Figure 7. (a) Pseudo-first-order model fit, (b) pseudo-second-order model fit, (c) Langmuir isotherms fitted, (d) Freundlich isotherms fitted.

Table 3. Fitted parameters of isotherm sorption models.

Adsorbate	$q_e(\text{exp})$ (mg/g)	Pseudo-First-Order Model			Pseudo-Second-Order Model		
		k_1 (min ⁻¹)	q_e (mg/g)	R^2	k_2 (g/mg · min ⁻¹)	q_e (mg/g)	R^2
SSN	Pb ²⁺	106.032	0.0088	0.9018	0.0106	94.3396	0.9901
	Cu ²⁺	62.212	0.0303	0.8478	0.0177	56.4972	0.9983

Langmuir and Freundlich isotherms were utilized to fit the linear regression sorption isotherm data according to the sorption experiments, and the results are shown in Figure 7c,d. And, as illustrated in Table 4, the correlation coefficient (R^2) of the Freundlich isotherm model is larger than the value of the Langmuir isotherm model. Apparently, the Freundlich isotherm exhibits a superior fit to the experimental data, which indicates that the adsorption of Pb^{2+} and Cu^{2+} cations onto the surface of SSN occurs through multilayer sorption [21]. In addition, the

theoretical maximum Pb^{2+} and Cu^{2+} sorption capacity by SSN was 185.2 mg/g and 86.2 mg/g. In addition, the Pb^{2+} and Cu^{2+} sorption capacity of different adsorbents synthesized from fly ash, as reported in previous articles and this study, are presented and compared in Table 5. These findings demonstrate the potential applicability of aminated SiO_2 synthesized from fly ash for the effective sorption of Pb^{2+} and Cu^{2+} .

Table 4. Fitted parameters of the isotherm sorption models.

Adsorbent	Adsorbate	Isotherm	Parameters	R^2
SSN	Pb^{2+}	Langmuir	$q_m = 185.1852 \text{ mg/g}, b = 0.0008 \text{ L/mg}$	0.9018
SSN	Pb^{2+}	Freundlich	$n = 1.3277, k_f = 2.7063$	0.9901
SSN	Cu^{2+}	Langmuir	$q_m = 86.2069 \text{ mg/g}, b = 0.0009 \text{ L/mg}$	0.8397
SSN	Cu^{2+}	Freundlich	$n = 1.6432, k_f = 2.2991$	0.9901

Table 5. Comparison of Pb^{2+} and Cu^{2+} sorption capacity of different fly ash-derived adsorbents.

	Adsorbate	Dosage (g/L)	pH	$q_e/(\text{mg/g})$	Ref
Activated coal fly ash	Pb^{2+}	4	3.0	49.8	[37]
Silica synthesized from fly ash	Pb^{2+}	1	5.0	90.0	[6]
NaOH- activated-coal fly ash	Pb^{2+}	2	5.0	126.6	[38]
Aminated spherical SiO_2 synthesized from fly ash	Pb^{2+}	1	Natural pH	185.2	This work
Fly ash/magnetite material	Cu^{2+}	10	5.0	17.4	[39]
Fly ash/steel slag-based geopolymers	Cu^{2+}	2	Natural pH	38.4	[40]
Fly ash-derived calcium silicate hydrate	Cu^{2+}	1	Natural pH	57.8	[13]
Aminated spherical SiO_2 synthesized from fly ash	Cu^{2+}	1	Natural pH	86.2	This work

Recycling Performance of SSN

The recycling performance of SSN was assessed through cyclic sorption–desorption experiments, using Pb^{2+} and Cu^{2+} solutions, with a concentration of 200 mg/L. The dosage of SSN for Pb^{2+} sorption was fixed at 4 g/L, while for Cu^{2+} sorption it was set at 6 g/L. After each sorption cycle, the Pb^{2+} (or Cu^{2+}) adsorbed by SSN was separated with heavy metal cations using the following process: filtration, immersion, and stirring of 0.1 mol/L HNO_3 for 1 h, deionized water filtration, and final drying at 60 °C for 8 h. As shown in Figure 8, the sorption efficiency decreases after an increase in the cycle number. After four iterations of the sorption–desorption process, the sorption efficiency of Pb^{2+} and Cu^{2+} decreased to 49.0% and 33.3%, which might be attributed to the loss of active adsorption sites in the sorption–desorption process, as well as the pore structure collapse caused by the acidic solution that would weaken the sorption ability [18,41].

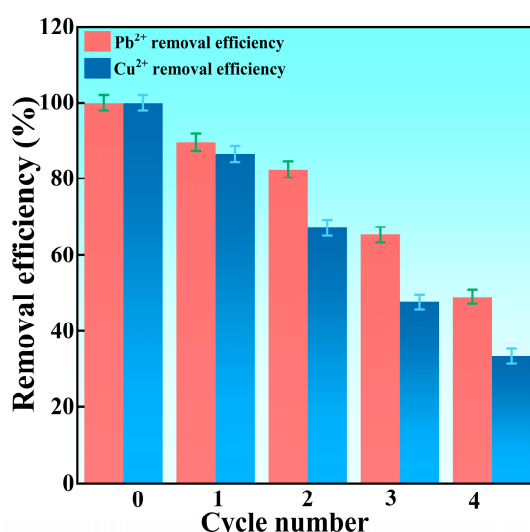


Figure 8. Recycling ability of SSN.

3.3. Mechanisms for Sorption

The FTIR spectra of SSN, SSN-Pb, and SSN-Cu (the Pb^{2+} and Cu^{2+} adsorbed SSN) are presented in Figure 9. Accordingly, the adsorption strength of the characteristic peaks assigned to the $-\text{NH}_2$ groups (at 1539 cm^{-1}) were weakened, which might be due to the complex reaction between the nitrogen atoms and the Pb^{2+} (or Cu^{2+}) cations [18]. In addition, the weakening of the characteristic peaks for $-\text{NH}-$ (694 cm^{-1}), C–N (1350 cm^{-1}), and $-\text{CH}_2-$ was due to the surface-covering Pb (or Cu) atoms in the adsorbent [9,29]. Obviously, the nitrogen-containing functional groups were the key active sites for Pb^{2+} and Cu^{2+} sorption.

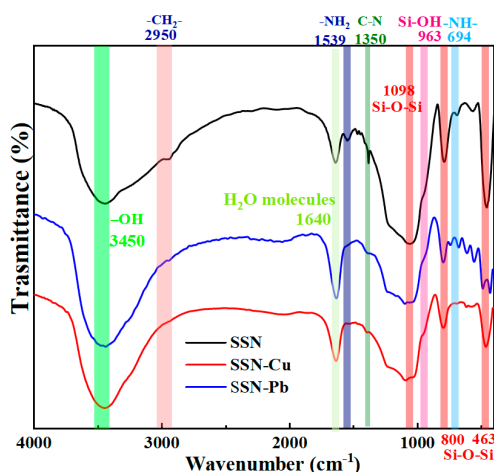


Figure 9. FTIR spectra of SSN, SSN-Pb, and SSN-Cu.

The XPS analysis was run for SSN, SSN-Pb, and SSN-Cu to determine the surface chemical environment of the elemental composition for N, Pb, and Cu, and the results are shown in Figure 10. The characteristic peaks of Pb 4f and Cu 2p are visibly observed for SSN-Pb and SSN-Cu, respectively (Figure 10a–c), indicating that the Pb and Cu cations have attached to the surface of SSN. In addition, the characteristic peaks of the $-\text{NH}_3^+$ (401.94 eV) and $-\text{NH}_2$ (399.74 eV) groups in the N 1s pattern (Figure 10d) had shifted slightly in terms of higher energy, which could be attributed to the complex reaction between these nitrogen-containing groups and the heavy metal cations [17]. The weakening of the adsorption peak for the $-\text{NH}-$ group (694 eV) was attributed to the surface-covering Pb (or Cu) atoms in the adsorbent. These findings illustrate that $-\text{NH}_3^+$ and $-\text{NH}_2$ groups play a key role in Pb^{2+} and Cu^{2+} sorption.

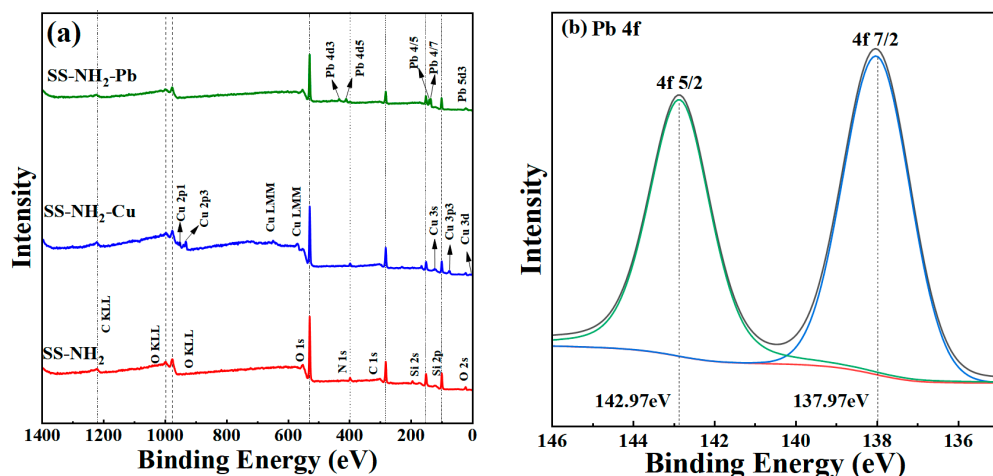


Figure 10. Cont.

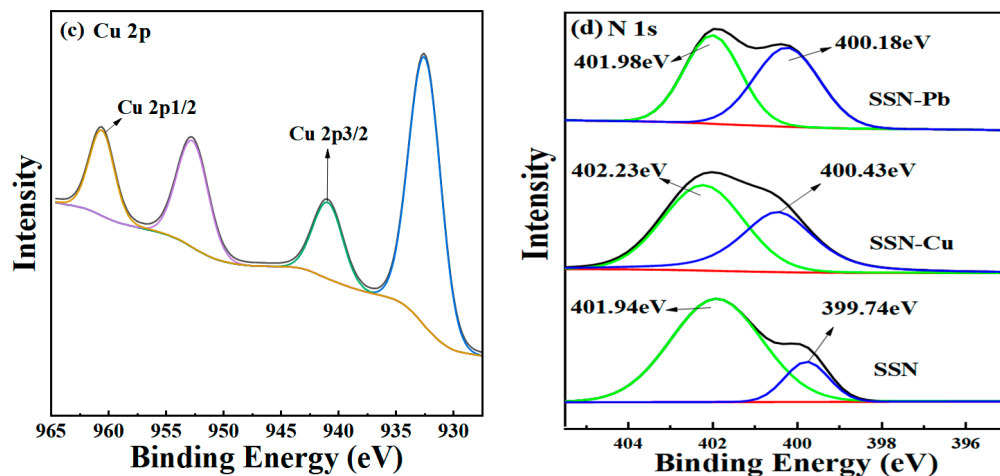
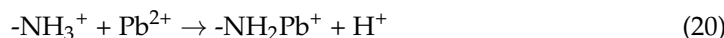


Figure 10. XPS spectra of SSN, SSN-Pb, and SSN-Cu: (a) XPS spectra, (b) Pb 4f of SSN-Pb, (c) Cu 2p of SSN-Cu, (d) N 1s spectra.

Therefore, the proposed Pb^{2+} and Cu^{2+} sorption mechanisms by SSN were as follows: In the sorption process, the surface Si-OH groups were deionized first and became negatively charged (as in Equation (7)), which attracted the heavy metal cations (Pb^{2+} and Cu^{2+}) to the surface of the adsorbent. Meanwhile, the $-\text{NH}_2$ groups were protonated to form $-\text{NH}_3^+$ (as in Equation (8)). Subsequently, the $-\text{NH}_3^+$ groups were involved in the ion exchange with the Pb^{2+} and Cu^{2+} cations in order to fix them on the SSN (as in Equations (20) and (21)) [32,42]. Although the $-\text{NH}_3^+$ groups showed electrostatic repulsion to Pb^{2+} and Cu^{2+} , the electrostatic attraction from $\text{Si}-\text{O}^-$ could secure the Pb^{2+} and Cu^{2+} cations to the surface of the SSN, which made these chemical reactions possible. In sum, despite that the $\text{Si}-\text{O}^-$ groups could attract heavy metal cations, they lacked the ability to fix them, thus they had a poor sorption ability in regard to pure SiO_2 . In contrast, the ammoniation modification process had provided abundant nitrogen-containing active sites, so that SSN had the complete ability to attract and fix heavy metal cations and, thus, had efficient Pb^{2+} and Cu^{2+} removal ability.



4. Conclusions

Spherical SiO_2 (SS), with a high specific surface area ($677.5 \text{ m}^2/\text{g}$) and pore volume ($0.23 \text{ cm}^3/\text{g}$), was synthesized from fly ash, and it was ammonified by APTES ($\text{H}_2\text{NCH}_2\text{CH}_2\text{CH}_2\text{Si}(\text{OC}_2\text{H}_5)_3$) to obtain the aminated spherical SiO_2 (SSN) in this work. According to the characterization analysis, nitrogen-containing groups ($-\text{NH}_3^+$, $-\text{NH}_2$, and $-\text{NH}$) were successfully introduced into the spherical SiO_2 without damaging its spherical structure, which significantly improved the Pb^{2+} and Cu^{2+} sorption ability. As a result of the Langmuir model, the theoretical maximum Pb^{2+} and Cu^{2+} sorption capacity of SSN was 185.2 mg/g and 86.2 mg/g . Moreover, the removal efficiency for Pb^{2+} and Cu^{2+} stayed at 49.0% and 33.3% after the cyclic sorption–desorption process was repeated four times. The efficient Pb^{2+} and Cu^{2+} sorption ability was ascribed to the nitrogen-containing groups. This work provides a strategy for utilizing solid waste as raw material to prepare aminated SiO_2 for the removal of Pb^{2+} and Cu^{2+} from water.

Author Contributions: J.C.: writing original draft, investigation, data curation, validation. N.L.: conceptualization, methodology, writing-review and editing, funding acquisition, supervision. Y.W.: visualization, data curation, formal analysis. X.L.: visualization, data curation, formal analysis. Z.Z.: data curation, resources. L.L.: data curation, resources. Z.D.: data curation, resources. S.H.: conceptualization, methodology, funding acquisition. All authors have read and agreed to the published version of the manuscript.

Funding: This research received no external funding.

Data Availability Statement: Data is contained within the article.

Conflicts of Interest: The authors declare no conflict of interest.

References

- Rahman, A. Promising and Environmentally Friendly Removal of Copper, Zinc, Cadmium, and Lead from Wastewater Using Modified Shrimp-Based Chitosan. *Water* **2024**, *16*, 184. [[CrossRef](#)]
- Shah, K.J.; Yu, J.; Zhang, T.; You, Z. Y-Type Zeolite Synthesized from an Illite Applied for Removal of Pb(II) and Cu(II) Ions from Aqueous Solution: Box-Behnken Design and Kinetics. *Water* **2023**, *15*, 1171. [[CrossRef](#)]
- Wadhawan, S.; Jain, A.; Nayyar, J.; Mehta, S.K. Role of nanomaterials as adsorbents in heavy metal ion removal from waste water: A review. *J. Water Process Eng.* **2019**, *33*, 101038. [[CrossRef](#)]
- Guimarães, T.G.S.; Barros, L.A.; Silva, R.S.; Gonzalez, M.H.; Carrilho, E.N.V.M.; Labuto, G. Synthesis and characterization of biochars modified with natural deep eutectic solvent (NADES) for dipyrone removal from aqueous medium. *Sustain. Chem. Pharm.* **2023**, *35*, 101205. [[CrossRef](#)]
- Shafiq, M.; Alazba, A.A.; Amin, M.T. Preparation of ZnMgAl-Layered Double Hydroxide and Rice Husk Biochar Composites for Cu(II) and Pb(II) Ions Removal from Synthetic Wastewater. *Water* **2023**, *15*, 2207. [[CrossRef](#)]
- Zhang, X.; Zhu, Z. Lead sorption performance on active silica derived from fly ash. *Water Sci. Technol.* **2015**, *71*, 661–666. [[CrossRef](#)]
- Zeng, Q.; Huang, Y.; Huang, L.; Hu, L.; Sun, W.; Zhong, H.; He, Z. High adsorption capacity and super selectivity for Pb(II) by a novel adsorbent: Nano humboldtine/almandine composite prepared from natural almandine. *Chemosphere* **2020**, *253*, 126650. [[CrossRef](#)] [[PubMed](#)]
- Zhang, Y.; Luo, J.; Feng, B.; Xu, H.; Sun, Y.; Gu, X.; Hu, X.; Naushad, M.; Gao, B.; Ren, H. Delamination of multilayer Ti₃C₂T_x MXene alters its adsorptivity and reduction of heavy metals in water. *Environ. Pollut.* **2023**, *330*, 121777. [[CrossRef](#)] [[PubMed](#)]
- Wang, Z.; Xu, L.; Su, N.; Zhu, S.; Wu, D. Preparation of amino-functionalized fly ash based tobermorite for enhanced removal of Cr(VI). *Environ. Sci. Pollut. Res.* **2023**, *30*, 54547–54555. [[CrossRef](#)] [[PubMed](#)]
- Li, Z.; Qian, W.; Chen, Y.; Xu, P.; Li, J.; Yang, J. A new treasure in industrial solid waste—Coal fly ash for effective oil/water separation. *J. Taiwan Inst. Chem. Eng.* **2020**, *118*, 196–203. [[CrossRef](#)]
- Pattanaik, S.; Parhi, P.K.; Das, D.; Samal, A.K. Acacia concinna: A natural dispersant for stabilization and transportation of fly ash-water slurry. *J. Taiwan Inst. Chem. Eng.* **2019**, *99*, 193–200. [[CrossRef](#)]
- Misran, H.; Singh, R.; Begum, S.; Yarmo, M.A. Processing of mesoporous silica materials (MCM-41) from coal fly ash. *J. Mater. Process. Technol.* **2007**, *186*, 8–13. [[CrossRef](#)]
- Joseph, I.V.; Tosheva, L.; Doyle, A.M. Simultaneous removal of Cd(II), Co(II), Cu(II), Pb(II), and Zn(II) ions from aqueous solutions via adsorption on FAU-type zeolites prepared from coal fly ash. *J. Environ. Chem. Eng.* **2020**, *8*, 103895. [[CrossRef](#)]
- Guo, Y.; Tan, C.; Wang, P.; Sun, J.; Yan, J.; Li, W.; Zhao, C.; Lu, P. Kinetic study on CO₂ adsorption behaviors of amine-modified co-firing fly ash. *J. Taiwan Inst. Chem. Eng.* **2018**, *96*, 374–381. [[CrossRef](#)]
- Liu, X.; Liu, N.; Li, X.; Luo, Y.; Li, X.; Hu, B.; He, X.; Liu, C.; He, S. Effect of aluminum modified mesoporous SBA-15 on surface properties and arsenic adsorption performance. *J. Porous Mater.* **2022**, *30*, 127–140. [[CrossRef](#)]
- McManamon, C.; Burke, A.M.; Holmes, J.D.; Morris, M.A. Amine-functionalised SBA-15 of tailored pore size for heavy metal adsorption. *J. Colloid Interface Sci.* **2011**, *369*, 330–337. [[CrossRef](#)] [[PubMed](#)]
- Wang, C.; Xie, J.; Zheng, M.; Zhu, J.; Shi, C. Preparation of Mesoporous Biochar from Cornstalk for the Chromium (VI) Elimination by Using One-Step Hydrothermal Carbonation. *J. Anal. Methods Chem.* **2021**, *2021*, 3418887. [[CrossRef](#)] [[PubMed](#)]
- Jiang, S.; Yan, L.; Wang, R.; Li, G.; Rao, P.; Ju, M.; Jian, L.; Guo, X.; Che, L. Recyclable nitrogen-doped biochar via low-temperature pyrolysis for enhanced lead(II) removal. *Chemosphere* **2021**, *286*, 131666. [[CrossRef](#)] [[PubMed](#)]
- Kasera, N.; Kolar, P.; Hall, S.G. Nitrogen-doped biochars as adsorbents for mitigation of heavy metals and organics from water: A review. *Biochar* **2022**, *4*, 17. [[CrossRef](#)]
- Cheng, S.; Zhao, S.; Guo, H.; Xing, B.; Liu, Y.; Zhang, C.; Ma, M. High-efficiency removal of lead/cadmium from wastewater by MgO modified biochar derived from crofton weed. *Bioresour. Technol.* **2021**, *343*, 126081. [[CrossRef](#)] [[PubMed](#)]
- Zhou, N.; Chen, H.; Feng, Q.; Yao, D.; Chen, H.; Wang, H.; Zhou, Z.; Li, H.; Tian, Y.; Lu, X. Effect of phosphoric acid on the surface properties and Pb(II) adsorption mechanisms of hydrochars prepared from fresh banana peels. *J. Clean. Prod.* **2017**, *165*, 221–230. [[CrossRef](#)]

22. Jung, K.-W.; Lee, S.Y.; Choi, J.-W.; Lee, Y.J. A facile one-pot hydrothermal synthesis of hydroxyapatite/biochar nanocomposites: Adsorption behavior and mechanisms for the removal of copper(II) from aqueous media. *Chem. Eng. J.* **2019**, *369*, 529–541. [[CrossRef](#)]
23. Li, X.; Hu, B.; Liu, N.; Liu, X.; Liu, C.; He, X.; He, S. Extraction of alumina from high-alumina fly ash by ammonium sulfate: Roasting kinetics and mechanism. *RSC Adv.* **2022**, *12*, 33229–33238. [[CrossRef](#)]
24. Wang, J.; Zhao, W.; Li, Z.; Ding, K.; Jin, Z. Investigation on into the adsorption of Cu(II), Pb(II) and Cr(VI) on hollow mesoporous silica using microcalorimetry. *J. Therm. Anal. Calorim.* **2019**, *137*, 1443–1450. [[CrossRef](#)]
25. Alsalbokh, M.; Fakeri, N.; Lawson, S.; Rownaghi, A.A.; Rezaei, F. Adsorption of iodine from aqueous solutions by aminosilane-grafted mesoporous alumina. *Chem. Eng. J.* **2021**, *415*, 128968. [[CrossRef](#)]
26. Li, Y.; Li, T.; Jin, Z. Stabilization of FeO nanoparticles with silica fume for enhanced transport and remediation of hexavalent chromium in water and soil. *J. Environ. Sci.* **2011**, *23*, 1211–1218. [[CrossRef](#)]
27. Fang, W.; Jiang, X.; Luo, H.; Geng, J. Synthesis of graphene/SiO₂@polypyrrole nanocomposites and their application for Cr(VI) removal in aqueous solution. *Chemosphere* **2018**, *197*, 594–602. [[CrossRef](#)] [[PubMed](#)]
28. Mahdavi, H.; Ahmadian-Alam, L.; Molavi, H. Grafting of sulfonated monomer onto an amino-silane functionalized 2-aminoterephthalate metal – organic framework via surface-initiated redox polymerization: Proton-conducting solid electrolytes. *Polym. Int.* **2015**, *64*, 1578–1584. [[CrossRef](#)]
29. Zhang, Z.; Liu, N.; Li, X.; Wang, Y.; Xiong, Y.; Meng, R.; Liu, L.; He, S. Single-step hydrothermal synthesis of biochar from waste industrial hemp stalk core for Pb²⁺ sorption: Characterization and mechanism studies. *Sustain. Chem. Pharm.* **2023**, *36*, 101316. [[CrossRef](#)]
30. Kang, S.; Chung, Y.G.; Kang, J.H.; Song, H. CO₂ absorption characteristics of amino group functionalized imidazolium-based amino acid ionic liquids. *J. Mol. Liq.* **2019**, *297*, 111825. [[CrossRef](#)]
31. Bao, S.; Yang, W.; Wang, Y.; Yu, Y.; Sun, Y.; Li, K. PEI grafted amino-functionalized graphene oxide nanosheets for ultrafast and high selectivity removal of Cr(VI) from aqueous solutions by adsorption combined with reduction: Behaviors and mechanisms. *Chem. Eng. J.* **2020**, *399*, 125762. [[CrossRef](#)]
32. Luo, L.; Cheng, S.; Yue, L.; You, Z.; Cai, J. N-doped biochar from chitosan gel-like solution: Effect of hydrothermal temperature and superior aqueous Cr (VI) removal performance. *Colloids Surf. A* **2022**, *641*, 128426. [[CrossRef](#)]
33. Han, C.; Xie, J.; Wei, K.; Liang, L.; Yang, T.; He, S.; Shi, Q. Simultaneous removal of Rhodamine B and Cu(II) by FeO(1 1 0)-decorated ZSM-5: Cu(II) role, reactivity and mechanism. *Chem. Eng. Sci.* **2023**, *282*, 119225. [[CrossRef](#)]
34. Xia, Y.; Yang, T.; Zhu, N.; Li, D.; Chen, Z.; Lang, Q.; Liu, Z.; Jiao, W. Enhanced adsorption of Pb(II) onto modified hydrochar: Modeling and mechanism analysis. *Bioresour. Technol.* **2019**, *288*, 121593. [[CrossRef](#)] [[PubMed](#)]
35. Sun, L.; Wu, J.; Wang, J.; Xu, M.; Zhou, W.; Du, Y.; Li, Y.; Li, H. Fabricating hydroxyapatite functionalized biochar composite using steel slag and Hami melon peel for Pb(II) and Cd(II) removal. *Colloids Surf. A* **2023**, *666*, 131310. [[CrossRef](#)]
36. Zhu, F.; Li, L.; Xing, J. Selective adsorption behavior of Cd(II) ion imprinted polymers synthesized by microwave-assisted inverse emulsion polymerization: Adsorption performance and mechanism. *J. Hazard. Mater.* **2016**, *321*, 103–110. [[CrossRef](#)]
37. Liu, Y.; Yan, C.; Zhang, Z.; Wang, H.; Zhou, S.; Zhou, W. A comparative study on fly ash, geopolymers and faujasite block for Pb removal from aqueous solution. *Fuel* **2016**, *185*, 81–189. [[CrossRef](#)]
38. Huang, X.; Zhao, H.; Zhang, G.; Li, J.; Yang, Y.; Ji, P. Potential of removing Cd(II) and Pb(II) from contaminated water using a newly modified fly ash. *Chemosphere* **2019**, *242*, 125148. [[CrossRef](#)] [[PubMed](#)]
39. Harja, M.; Buema, G.; Lupu, N.; Chiriac, H.; Herea, D.D.; Ciobanu, G. Fly Ash Coated with Magnetic Materials: Improved Adsorbent for Cu (II) Removal from Wastewater. *Materials* **2020**, *14*, 63. [[CrossRef](#)] [[PubMed](#)]
40. Yan, S.; Feng, X.; Huang, K.; Ren, X.; Zhao, Y.; Xing, P. Synthesis and adsorption performance of fly ash/steel slag-based geopolymers for removal of Cu (II) and methylene blue. *Int. J. Appl. Ceram. Technol.* **2023**, *20*, 1591–1605. [[CrossRef](#)]
41. Zhang, J.; Hu, X.; Zhang, K.; Xue, Y. Desorption of calcium-rich crayfish shell biochar for the removal of lead from aqueous solutions. *J. Colloid Interface Sci.* **2019**, *554*, 417–423. [[CrossRef](#)] [[PubMed](#)]
42. Yin, W.; Zhang, W.; Zhao, C.; Xu, J. Evaluation of Removal Efficiency of Ni(II) and 2,4-DCP Using in Situ Nitrogen-Doped Biochar Modified with Aquatic Animal Waste. *ACS Omega* **2019**, *4*, 19366–19374. [[CrossRef](#)] [[PubMed](#)]

Disclaimer/Publisher’s Note: The statements, opinions and data contained in all publications are solely those of the individual author(s) and contributor(s) and not of MDPI and/or the editor(s). MDPI and/or the editor(s) disclaim responsibility for any injury to people or property resulting from any ideas, methods, instructions or products referred to in the content.